

Independent Optical Frequency Combs Powered 546 km Field Test of Twin-Field Quantum Key Distribution

Lai Zhou,^{1,*} Jinping Lin,¹ Chengfang Ge,¹ Yuanbin Fan,¹ and Zhiliang Yuan^{1,†}

¹*Beijing Academy of Quantum Information Sciences, Beijing 100193, China*

Hao Dong,^{2,3,*} Yang Liu,^{3,4} Di Ma,³ Jiu-Peng Chen,^{2,3,4} Cong Jiang,^{3,4}
Xiang-Bin Wang,^{3,5,4} Li-Xing You,⁶ Qiang Zhang,^{2,3,4} and Jian-Wei Pan^{2,4}

²*Hefei National Research Center for Physical Sciences at the Microscale and School of Physical Sciences,
University of Science and Technology of China, Hefei, 230026, Anhui, China*

³*Jinan Institute of Quantum Technology and CAS Center for Excellence in Quantum Information and Quantum Physics,
University of Science and Technology of China, Jinan, 250101, Shandong, China*

⁴*Hefei National Laboratory, University of Science and Technology of China, Hefei, 230088, Anhui, China*

⁵*State Key Laboratory of Low Dimensional Quantum Physics,
Department of Physics, Tsinghua University, Beijing 100084, China*

⁶*Shanghai Key Laboratory of Superconductor Integrated Circuit Technology,
Shanghai Institute of Microsystem and Information Technology,
Chinese Academy of Sciences, Shanghai 200050, China*

(Dated: November 22, 2024)

Owing to its repeater-like rate-loss scaling, twin-field quantum key distribution (TF-QKD) has repeatedly exhibited in laboratory its superiority for secure communication over record fiber lengths. Field trials pose a new set of challenges however, which must be addressed before the technology's roll-out into real-world. Here, we verify in field the viability of using independent optical frequency combs—installed at sites separated by a straight-line distance of 300 km—to achieve a versatile TF-QKD setup that has no need for optical frequency dissemination and thus enables an open and network-friendly fiber configuration. Over 546 and 603 km symmetric links, we record a finite-size secure key rate (SKR) of 0.53 bit/s and an asymptotic SKR of 0.12 bit/s, respectively. Of practical importance, the setup is demonstrated to support 44 km fiber asymmetry in the 452 km link. Our work marks an important step towards incorporation of long-haul fiber links into large quantum networks.

I. INTRODUCTION

Unveiled in 1984 [1], quantum key distribution (QKD) is a revolutionary means for exchanging cryptographic keys over fiber networks [2–7]. Forty years later, it has emerged as a practical, and arguably the only known future-proof, candidate to mitigate imminent threats posed by quantum computers towards existing public-key infrastructures. The technology has been demonstrated in laboratory capable of delivering 10-100 Mbit/s secure key rates (SKR's) [8–10] and long-haul reach up to 421 km over a continuous fiber link [11]. Excitingly, using elegant ideas of twin-field (TF) [12] or post-measurement pairing [13, 14], fiber distances exceeding 500 km can now be routinely achieved [15–20] while achieving measurement-device-independent (MDI) security [21].

Long-distance links are highly desirable for deployment in a large-scale QKD network because they can reduce the number of trusted nodes and enhance overall network security. To this end, TF-QKD is an attractive choice.

Its viability for field use has recently been tested in early trials [22–24], with the longest fiber of 511 km linking two cities [23]. These trials successfully overcome TF-QKD's technical challenge for stabilizing and/or tracking the differential phase between laser fields transmitted from remote locations. However, the underlying solutions require either the communication users cloning a common laser frequency [22, 24] or calibrating their laser frequencies at regular intervals [23]. An auxiliary channel for frequency dissemination is then necessary, which results to a closed-loop fiber configuration and will thus restrict flexibility towards a scalable and switchable network.

Optical frequency comb (OFC) is emerging as a powerful technique for TF-QKD [18, 24]. Inter-wavelength coherence it brings enables dual-band stabilization [16] to function over fiber asymmetry of 10's kilometers, as field-trialed in a closed-loop fiber configuration [24]. Further, adoption of electro-optic combs removes the need for optical frequency dissemination and allows TF-QKD's operation over an open quantum channel [18], thus reducing its fiber complexity to the same level as MDI-QKD [21]. However, TF-QKD over an open quantum channel has yet to be demonstrated in a field environment nor has an OFC-powered setup delivered a positive SKR.

Here, we place the OFC powered technology under stringent field test and experimentally verify the viabil-

* Equal contribution.

† yuanzl@baqis.ac.cn

* Equal contribution.

ity of the TF-QKD setup we implemented to operate across a deployed 427 km link. Over symmetric quantum channels achieved by adding extra fiber spools, the setup is verified capable of delivering a finite-size SKR of 0.53 bit/s at 546 km and an asymptotic SKR of 0.12 bit/s at 603 km using the efficient TF-QKD variant of sending-not-sending (SNS) protocol [25, 26]. Furthermore, we demonstrate that the open channel scheme supports a large fiber asymmetry of 44 km in the 452 km asymmetric setup. This work proves TF-QKD’s operation without optical frequency dissemination in field and thus paves the way towards incorporation of long-haul links into secure quantum network.

II. FIELD EXPERIMENTAL SETUP

As shown in Fig. 1(a), the experimental setup is installed across three geographical sites connected by commercial fiber. The communication users (referred to as Alice and Bob) are placed at opposite ends of the fiber link, i.e., the metropolitan cities of Jinan and Qingdao, while the measurement node Charlie situates at Mazhan, a town that lies in the middle. The straight-line distance between Alice and Bob is 300 km. Two parallel fibers are allocated. The quantum fiber carrying the quantum signal has a total length of 427 km and is characterised to have a loss coefficient of 0.190 (0.185) dB km⁻¹ between Charlie and Alice (Bob). The synchronization fiber of the same length is dedicated for transmission of Charlie’s clock signal to time the users’ modulation units, see Fig. 1(b). Optical amplifiers are used to boost the clock signal in the synchronization fiber. Internet handles all other classical communications, which are not jitter-critical. To test quantum channels longer than 427 km, we add fiber spools (G654.C fiber) with a typical loss coefficient of 0.160 dB km⁻¹ at Charlie’s site.

Each user owns an independent OFC, made through 25 GHz microwave modulation to an ultra stable laser’s output, see Figs. 1(b, c). Precise comb spacing, crucial for this TF-QKD implementation, is ensured by referencing each 25 GHz microwave driver to a local Rubidium clock of an accuracy of 5×10^{-11} . Each OFC’s laser is locked to a high-finesse cavity to have a sub-Hertz short-term linewidth using Pound-Drever-Hall technique. Due to referencing to stable, independent cavities, two lasers are characterized to drift at a dominantly linear rate of 1.8 kHz/h, which is compensated for by adjusting the frequency offset in the locking path of Alice’s laser.

Each OFC generates 15 spectral lines, see Fig. 1(d). We choose 3 lines, in alignment with the ITU 50 GHz DWDM Grid, for carrying quantum ($\lambda_q = 1550.495$ nm, Ch 33.5), channel stabilization ($\lambda_c = 1549.694$ nm, Ch 34.5) and timing ($\lambda_t = 1549.293$ nm, Ch 35) signals, respectively. The λ_q light is carved and modulated into a sequence of blocks of 200 ns each, see Fig. 6 in Appendix B. Within each block, the first 100 ns comprises a train of 300 ps pulses clocked at 1 ns intervals and en-

coded to the single photon level to form the ‘quantum signal’, while in the remaining 100 ns centers one broad pulse of 70 ns duration serving as the ‘weak quantum reference’. The effective clock rate for quantum signal transmission is 500 MHz. The λ_c light is continuous-wave and serves as the ‘strong channel reference’, while the λ_t signal is carved into 10 MHz, 15 ns pulses and used as ‘time reference’ for Charlie to determine photon arrivals by his incoherent measurement unit (Fig. 1(b)).

Alice and Bob’s modulation units are timed with respective dynamical delays (Δt_A , Δt_B) to produce their quantum (λ_q) and time reference (λ_t) pulses by the incoming 50 MHz clock signal transmitted by Charlie through the synchronization fiber, see Fig. 9 in Appendix B. Its wavelength is chosen to be 1559.79 nm, spectrally distant from λ_q , to avoid cross-fiber noise [22, 23]. Polarizations of each user’s λ_c and λ_q signals are independently pre-compensated for by minimising the count rate at detectors D_2 and D_3 by adjusting the electric polarization controllers (EPCs) at the transmitter units, so that they are predominantly transmitted to Charlie’s coherent measurement unit through a polarization beam splitter (PBS), see Figs. 1(b,c). In the coherent measurement unit, the interference outcomes are demultiplexed in wavelength before entering detectors D_0 , D_1 and D_c . For more information on the experimental setup, refer to Appendix B.

III. FIELD TRIAL PREPARATION

The first task for the field trial is to align the OFC lasers to have their frequency difference within a confirmed active phase compensation bandwidth of ± 5 kHz. Using a fast photodiode and a frequency spectrum analyzer, we measure the beat frequency between the lasers at Mazhan after transmission from Jinan and Qingdao. Here, the users’ comb generation and modulation units are temporarily bypassed so as to ensure sufficient optical power entering the fast photodiode. Limited by fiber length fluctuation, we measure the beating frequency within an accuracy of ~ 2 kHz. This coarse result is sufficient for subsequent real-time frequency tracking via single photon detection.

We then reinstate the bypassed units into the setup. The intensities of Alice and Bob’s channel reference λ_c signals are set so that they are balanced and jointly produce 6 MHz count rate at Charlie’s phase detector (D_c in Fig. 1(b)). To stabilize the differential phase of the λ_c signals, a proportional–integral–derivative (PID) control module [18] is used to adjust the bias to Charlie’s phase modulator (PM) so as to stabilize the instantaneous count rate of D_c at 10 μ s intervals.

Figures 2(a₁) and 2(a₂) illustrate the effect of the λ_c locking on the phase drift of the quantum signal. Without this locking, fiber length fluctuation causes rapid, random drifts in the differential phase of the λ_q signal with a standard deviation of 1.65×10^4 rad/s, see

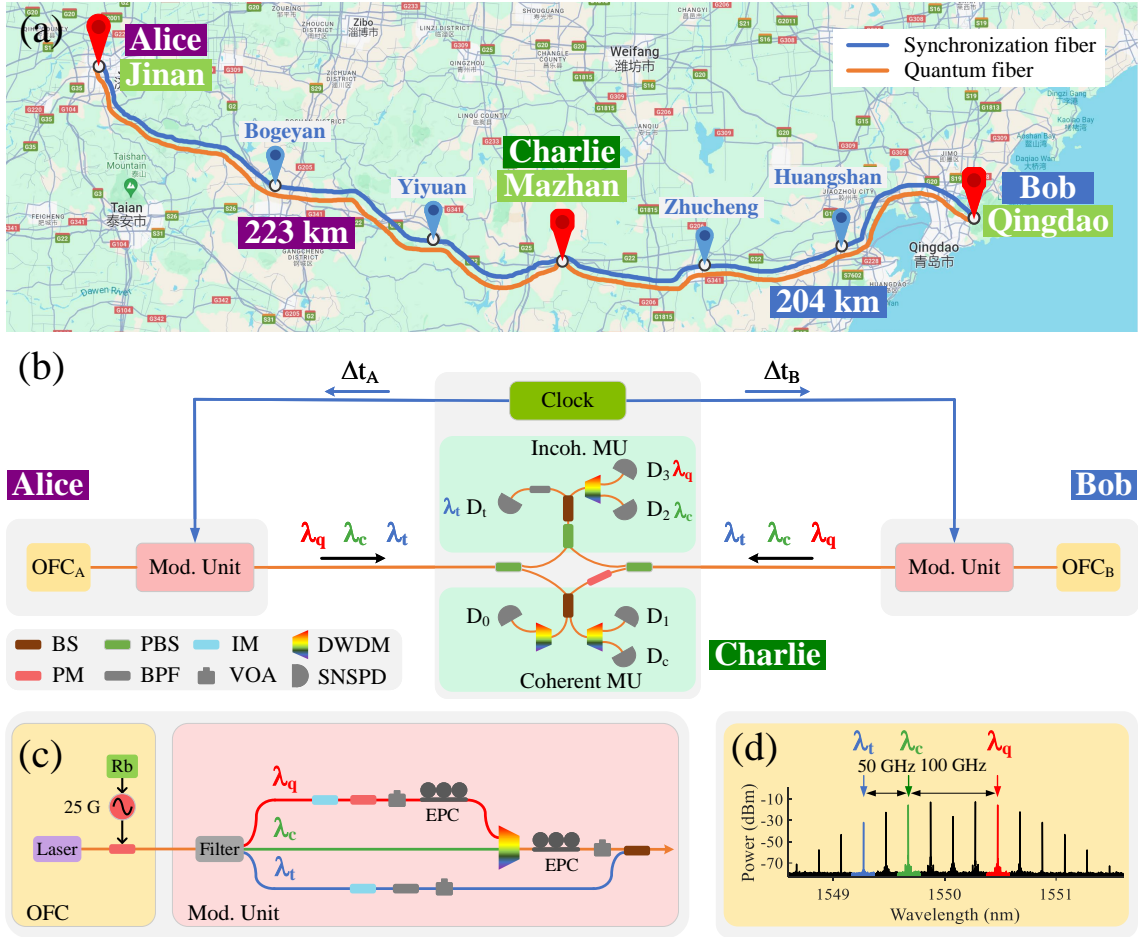


FIG. 1. Field test setup. (a) Deployed fiber route. (b) TF-QKD setup. (c) Transmitter, including OFC and Modulation Unit. (d) OFC spectrum. IM, intensity modulator; PM, phase modulator; BS, beam splitter; PBS, polarization beam splitter; DWDM, dense wavelength division multiplexer; SNSPD: superconducting nanowire single photon detector; EPC, electrically driven polarization controller; VOA, variable optical attenuator; BPF, band pass filter.

Fig. 2(a₁). This rate is similar to previously reported lab results over comparable fiber lengths [16, 17]. Locking the λ_c signal at 10 μ s intervals, the λ_q phase drift rate is slowed down by a factor of 220 with a standard deviation of 76 rad/s, see Inset of Fig. 2(a₁). The factor is 8.6 times less than the theoretical prediction [16] of $\lambda_c/|\lambda_c - \lambda_q| \simeq 1900$, and about 7 times poorer than recent lab operation [18]. The deterioration arises mainly from the use of two independent Rubidium clock references for OFCs, which have a specified accuracy of 5×10^{-11} each. With 100 GHz spacing between λ_c and λ_q , this accuracy translates to 44 rad/s residual phase drift. Turning on the λ_q phase locking, we measure a Gaussian distribution of 0.20 rad standard deviation for the residual phase, see Fig. 2(a₂). This residual phase spreads 1.5 times as much as in the laboratory result [18] and contributes 1% to the QBER in the X-basis. Please refer to Appendix B.4.b for details of the active phase stabilization.

Coherent dual-band stabilization allows real-time readout of the frequency offset based on the compensation sig-

nal on the PM [18]. Fig. 2(a₃) shows two readout results under different experimental conditions: with or without compensation of the linear offset drift turned on.

With phase and frequency drifts compensated for, the final preparation for the field trial is to maintain temporal alignment between Alice and Bob's quantum pulses. Their delays may vary more than 20 ns daily due to environmental temperature surrounding the fiber route. To correct, Charlie measures arrival times of Alice and Bob's λ_t pulses using detector D_t in his incoherent measurement unit (Fig. 1(b)) at 1 s intervals and then adjusts the time delay values of Δt_A and Δt_B accordingly. Figure 2(b₁) shows the delays that Charlie dynamically adjusts over a duration of 5 h. This dynamical adjustment ensures good temporal overlap between Alice and Bob's quantum signals as inferred from the jitters measured from their λ_t pulses, see Fig. 2(b₂). The jitter is measured to be just 8.4 ps, which is substantially smaller than the 300 ps duration of the quantum pulses and therefore does not exceedingly deteriorate the visibility

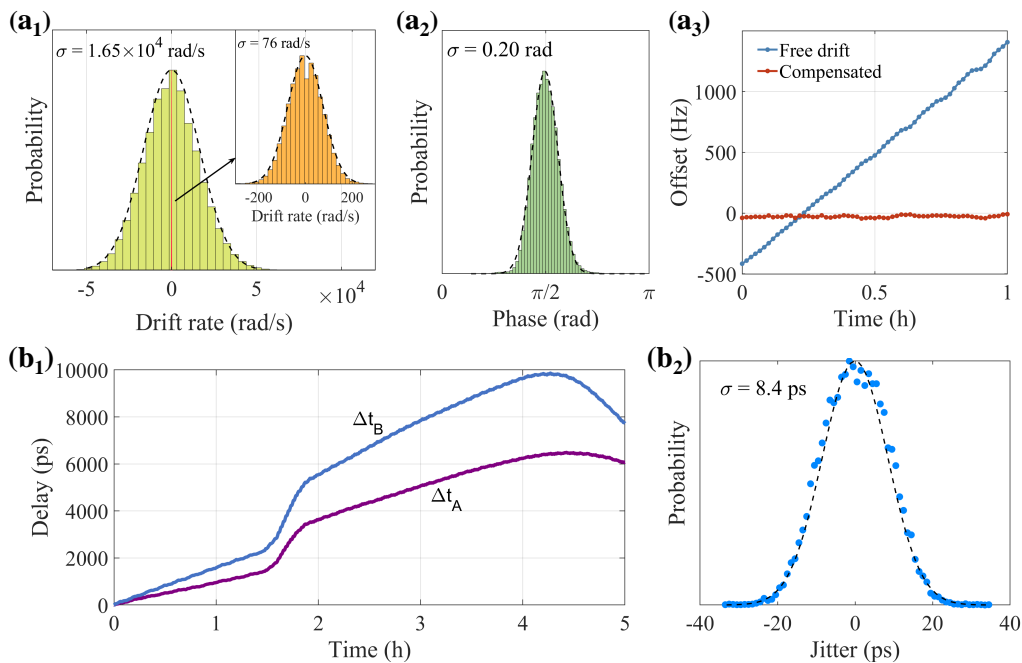


FIG. 2. Autonomous alignment for phase, optical frequency and arrival time. **a**, Coherent dual-band phase stabilization results; (a₁) Comparison for the phase drift rates of the quantum signal before (light green) and after (orange) turning on the fast phase compensation. Inset: Magnified view of the slowed phase drifts. (a₂) Phase angle distribution of the λ_q light with coherent dual-band stabilization fully on. (a₃) Readout of the laser frequency offset without (blue) and with (red) frequency compensation activated. **b**, Timing alignment using the incoherent measurement unit (MU). (b₁) Clock delays to Alice (purple) and Bob (blue); (b₂) Jitter distribution of the λ_t signals measured by Charlie. All data here were taken over the 427 km deployed fiber.

of the first-order interference. We measure a visibility of (97.95 ± 0.53) % for the quantum signal after coherent dual-band stabilization and transmission over the deployed fiber.

IV. RESULTS

We implement the sending-not-sending (SNS) TF-QKD protocol using 4 pulse intensities between two encoding bases [25, 26]. Each quantum pulse is encoded with a phase value, randomly selected from 16 phase slices, $\theta \in \{0, \pi/8, 2\pi/8 \dots 15\pi/8\}$, to meet the requirement of phase randomization and qubit encoding in TF-QKD protocol. In the Z-Basis, Alice and Bob independently choose at random whether or not send a pulse of a mean photon number of μ_Z for each transmission time slot, while the other three pulse intensities (μ_0, μ_1, μ_2 , and $\mu_0 < \mu_1 < \mu_2$) are used by each user in the X-Basis in order to apply decoy-state analysis to bound adversaries' information. The quantum bit error rate (QBER) in the raw bits, which are formed from events that Alice and Bob both chose the Z-Basis, is unaffected by the channel coherence. Instead, it is proportional to, and thus places a constraint on, the sending probability of μ_Z pulses. To address this issue, we apply the actively odd-parity pairing (AOPP) technique [27] in the data post-processing

and subsequently use the zig-zag approach [28] to ensure a high SKR with finite-size effects taken into account of. More information on the SNS-AOPP protocol is summarized in Appendix A.

We run the SNS-AOPP protocol over three quantum channel lengths. For 500 km or longer, we choose symmetric configuration for optimal performance distance-wise, in which Alice and Bob's transmission distances (losses) to Charlie are strictly matched. At 546.61 and 603.87 km, the link losses are respectively 100.13 and 108.59 dB. For the shortest distance of 452.46 km, we opt for a channel asymmetry of 44 km in order to demonstrate TF-QKD's adaptability to real network scenarios. At each distance, we transmit at least 4×10^{12} quantum pulses, corresponding to 2.22 h experimental time, for obtaining a statistically reliable measurement data set. For 546.61 km, the amount of quantum pulses is enlarged 6-fold to 2.772×10^{13} in order to rigorously account for finite-size effects. Protocol settings and measurement results are summarized in Tables V and VI in Appendix C.

Figure 3 plots experimentally measured SKR's (red symbols) as a function of quantum channel length, alongside which we include theoretical simulations that were obtained with two parameter sets corresponding to the experiments. In obtaining the finite-size (solid black) and asymptotic (dashed) simulation lines, we adopted experimentally measured values of an attenuation coefficient of 0.183 dB/km for the quantum channel and a detec-

tion efficiency of 0.66 averaged over detectors D_0 and D_1 . As shown in Fig. 3, experimental data for the symmetrical experiments are in excellent agreement with their respective simulations. For 603.87 km, the experiment is restricted to the asymptotic case by the access time to the fiber.

After tests over symmetrical channels, we move to an asymmetric configuration to further verify the robustness of our TF-QKD implementation. In this last trial, just a single 25 km fiber spool is placed into Alice's fiber path on top of the deployed 427 km link, and the distance between Charlie and Alice (Bob) is 248.24 km (204.22 km), extending the link asymmetry to 44 km (9.08 dB) in length (loss). The length of the spooled fiber is less than 1/4 of those used in the last two experiments, and thus the quantum channel becomes less susceptible to mechanical vibration in Charlie's server room. With help of further securing loose fiber cables, the final X-Basis QBER is reduced to 6.87 % from > 8.0 % found in the above symmetrical experiments. We obtain an asymptotic SKR of 24.28 bit/s at the distance of 452.46 km, as shown in Fig. 3. Compared with the theoretical simulation (dashed line), the rate does not exhibit a penalty expected for the fiber asymmetry. This is because the improvement in the X-basis QBER balances out the penalty. With a transmission of 4.28×10^{12} quantum pulses, we obtain a finite-size SKR of 16.06 bit/s.

To appreciate the advantage of TF-QKD, we compute the absolute repeaterless bound SKC_0 [29], which is the maximum SKR that an ideal point-point QKD system clocked at 500 MHz can offer. As shown in Fig. 3, all our experimental data points surpass their respective SKC_0 bound values, proving a repeater-like behavior of our system in field environment. At 452.46 and 546.61 km, the finite-size SKRs exceed their SKC_0 bounds by 6.45 and 7.57 times, respectively.

We compare in Fig. 3 our results with existing state-of-art long-haul field trials. Decoy-state BB84 feasibility study [30] or entanglement QKD [31] is limited to a distance of 250 km, primarily by the linear rate scaling [29] of conventional QKD protocols. On the other hand, TF-QKD field experiments [22, 23] fared substantially longer fiber spans, both exceeding 400 km, thanks to the protocol's intrinsic square-root scaling. Our setup further extends the communication distances to 546 km (100.13 dB) with finite-size effects included and 603 km (108.59 dB) for a positive asymptotic SKR. Moreover, it allows a link asymmetry of 44 km and features an open quantum link that brings ease to deployment. Finally, our result constitutes the first field trial that ever breaks 100 dB link loss barrier.

V. CONCLUSION

We have realized repeater-like quantum communication over field-deployed fibers of record length and loss. Our experiments demonstrate TF-QKD's viability to op-

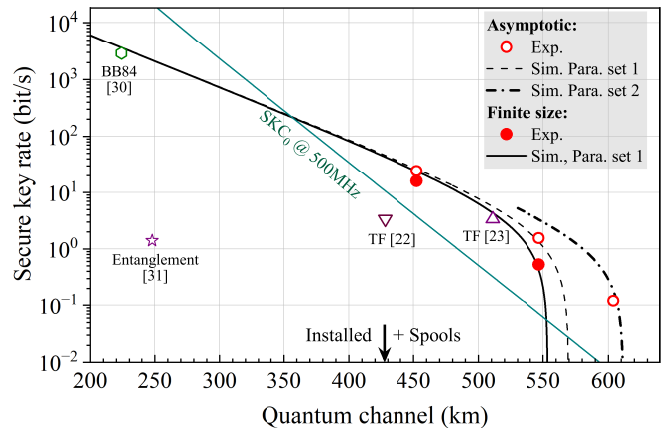


FIG. 3. Secure key rate results and simulations. According to experiments, two sets of simulation parameters are used. Set 1 (2): 0.660 (0.580) detector efficiency and 0.183 (0.180) dB/km fiber attenuation. The absolute repeaterless bound SKC_0 is calculated using 0.183 dB/km fiber attenuation. Previous field trials of decoy-state BB84 feasibility study [30], entanglement QKD [31] and TF-QKD [22, 23] are shown for comparison.

erate over an open quantum channel in a practical environment as well as its tolerance of channel asymmetry. This advance reduces TF-QKD's complexity for real-world deployment and thus makes it an attractive option to upgrade existing QKD networks. We believe our techniques will find applications in phase-sensitive quantum repeater and multinode quantum network [32, 33].

Several advances were made over our recent lab experiments [20], including incorporation of automated time alignment [23] and local clock references for OFCs. Autonomous time, frequency and phase alignment allows the system's sustaining operation at an effective clock rate of 500 MHz for quantum signal transmission, while local references have been demonstrated for the first time in quantum communication. In future, the performance of the coherent dual-band phase stabilization technique can be upgraded through use of clocks of higher accuracy [34] and/or detectors of higher count rates [35].

ACKNOWLEDGMENTS

This work was supported partially by the National Natural Science Foundation of China (62250710162, 62105034, 12374470, 12174215, T2125010, 61971409, 61971408), the Natural Science Foundation of Beijing (Z230005), the Innovation Program for Quantum Science and Technology (2021ZD0300700, 2023ZD0300100), the National Key R & D Plan of China (2020YFA0309800), the Key R&D Plan of Shandong Province (2021ZDPT01), and the Shandong Provincial Natural Science Foundation (ZR2022LLZ011). H.D., J.P.C., Q.Z. and J.W.P. acknowledge support from the Chinese Academy of Sciences. Q.Z. acknowl-

edges support from the Taishan Scholar Program of Shandong Province. Z.Y. acknowledges support from the ChangJiang Chair Scholars Program, Ministry of Education.

Appendix A: Protocol

In this experiment, we adopt the SNS-TF-QKD protocol [25] with 4-intensities [36], i.e., there are four phase-randomized weak coherent state (WCS) sources with different intensities in Alice and Bob's side respectively. For clarify, we denote the four sources in Alice's side by o_a, x_a, y_a, z_a and the four sources in Bob's side by o_b, x_b, y_b, z_b , whose intensities are $\mu_{a_l} (\mu_{b_l})$ for $l = 0, 1, 2, Z$. Specifically, the sources o_a, o_b are vacuum sources and $\mu_{a_0} = \mu_{b_0} = 0$. To get the highest key rate in the asymmetric channel, the asymmetric 4-intensity SNS-TF-QKD protocol is applied here [26]. Also, in the data post-processing stage, the actively odd-parity pairing (AOPP) is applied to reduce the bit-flip error rate and further improve the key rate [28, 37].

In this protocol, Alice and Bob would repeat the following process for N times: At each time window, Alice (Bob) randomly decides whether it is a decoy window with probability $1 - p_A$ ($1 - p_B$), or a signal window with

probability p_A (p_B). If it is a signal window, with probability ϵ_A (ϵ_B), Alice (Bob) chooses the source z_a (z_b), and denote it as bit 1 (0); with probability $1 - \epsilon_A$ ($1 - \epsilon_B$), Alice (Bob) chooses the source o_a (o_b), and denote it as bit 0 (1). If it is a decoy window, Alice (Bob) randomly choose the sources o_a, x_a, y_a (o_b, x_b, y_b) with probabilities $p_{a_0}, p_{a_1}, p_{a_2} = 1 - p_{a_0} - p_{a_1}$ ($p_{b_0}, p_{b_1}, p_{b_2} = 1 - p_{b_0} - p_{b_1}$) respectively. To ensure the security of the asymmetric protocol, the following condition is required

$$\frac{\mu_{a_1}}{\mu_{b_1}} = \frac{\epsilon_A(1 - \epsilon_B)\mu_{a_z}e^{-\mu_{a_z}}}{\epsilon_B(1 - \epsilon_A)\mu_{b_z}e^{-\mu_{b_z}}}. \quad (\text{A1})$$

Then Alice and Bob send their prepared pulses to Charlie who is assumed to perform interferometric measurements on the received pulses and then announces the results to Alice and Bob. If one and only one detector clicks in the measurement process, Charlie also tells Alice and Bob which detector it was, and Alice and Bob take it as a one-detector heralded event. After Alice and Bob repeat the above process for N times, they acquire a series of data, which are used to perform the data post-processing including the AOPP, the decoy-method analysis, the error correction and the privacy amplification to extract the final keys. And they can calculate the secure final key rate by the following formula:

$$R = \frac{1}{N} \{n'_1[1 - h(e_1^{ph})] - fn'_t h(E') - 2 \log_2 \frac{2}{\epsilon_{cor}} - 2 \log_2 \frac{1}{\sqrt{2}\epsilon_{PA}\hat{\epsilon}}\}, \quad (\text{A2})$$

where n'_1 is the number of the untagged bits after AOPP, e_1^{ph} is the bit flip error rate of untagged bits after AOPP, $h(x) = -x \log_2 x - (1 - x) \log_2 (1 - x)$ is the Shannon entropy, n'_t is the number of the remaining bits after AOPP, E' is the bit-flip error rate of the remaining bits after AOPP, ϵ_{cor} is the failure probability of error correction, ϵ_{PA} is the failure probability of privacy amplification, and $\hat{\epsilon}$ is the coefficient while using the chain rules of smooth minimal and maximal entropies [38]. The decoy analysis method to get n'_1 and e_1^{ph} are shown in Ref. [37]. For simplicity, we do not list the calculation details here.

Appendix B: Detailed description of experimental setup

With reference to the schematic shown in Fig. 4, we describe in detail our experimental setup with focus on optical frequency comb, modulation units, measurement units, drifts compensation and quantum channel characteristics. Alice and Bob's apparatus are largely identical, so only Bob's setup is shown in Fig. 4 to avoid repetition.

1. Optical frequency combs

In the experiment, we use two independent optical frequency combs (OFCs) that are realized through 25 GHz electro-optic modulation to ultra-stable lasers. For each OFC, its 25 GHz driver is referenced to a local Rubidium frequency standard of with a short-term (1 s) stability of 2×10^{-11} and an accuracy of 5×10^{-11} . The frequency accuracy of 5×10^{-11} causes an error of 5 Hz for 100 GHz span, which means a residual phase drift rate of 7.1 Hz for the quantum signal (λ_q) when the classical signal (λ_c) is perfectly phase stabilized.

The lasers in OFCs were from different manufacturers (Menlo Systems #ORS-Cubic and Stable Laser Systems #SLS-INT-1550-200-1), and both feature a sub-Hz short-term linewidth thanks to their use of Pound-Drever-Hall (PDH) technique for locking to a reference cavity. Before installation to their respective sites, the two lasers were characterised side by side in laboratory to have a relative linear differential frequency drift of 1777 Hz per hour, see Fig. 5. The Menlo laser is installed in a research laboratory with network fiber access in Jinan, while the other laser is installed into an equipment cabinet in one of China Unicom's data centers in Qingdao.

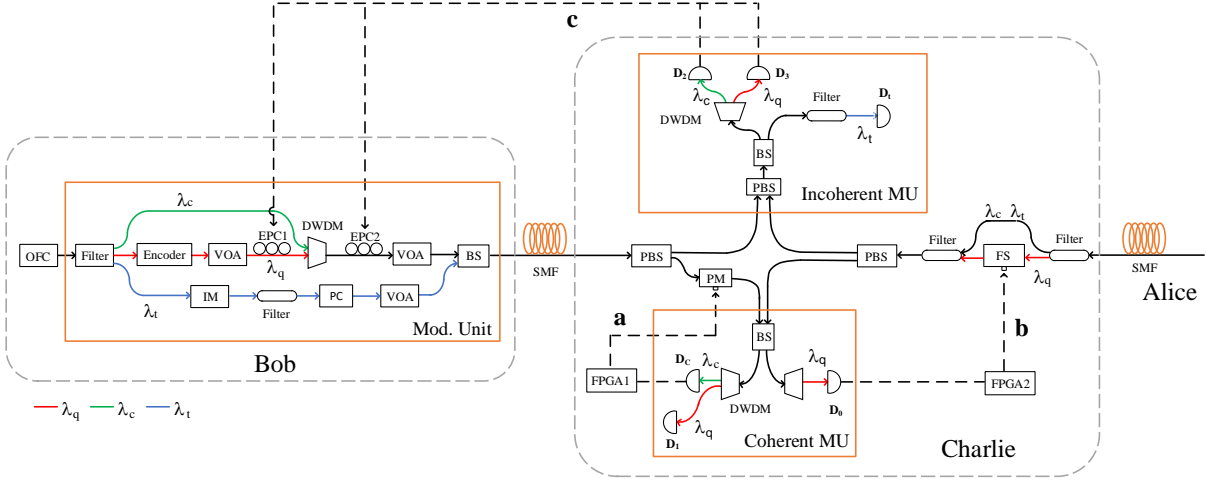


FIG. 4. Phase and polarization stabilization setup. **a**, Fast phase compensation module: FPGA1 is used to detect the counts from detector D_c and derive the error signal driving Charlie's phase modulator (PM) for phase compensation in channel reference λ_c . **b**, Slow phase compensation module: FPGA2 obtains the error signal from Detector D_0 and drives the fiber stretch (FS) for compensating the residual phase drift in the quantum reference λ_q . **c**, Polarization feedback module: EPC1 (EPC2) gets error signal from Detector D_3 (D_2) and calibrate the polarization drift in wavelength λ_q (λ_c). OFC: optical frequency comb; VOA: variable optical attenuator; IM: intensity modulator; BS: beam splitter; SMF: single mode fiber; PBS: polarization beam splitter/combiner; FPGA: field-programmable-gated-array; DWDM: dense wavelength division multiplexing; EPC: electrically driven polarization controller; PC: polarization controller; MU: measurement unit.

The Menlo laser has an electro-optical modulator in its PDH locking path so as to allow frequency tuning over the cavity free spectral range (FSR) and thus alignment of the two lasers' frequencies. Both lasers are aligned to 1550.094 nm and output 20 mW of power each.

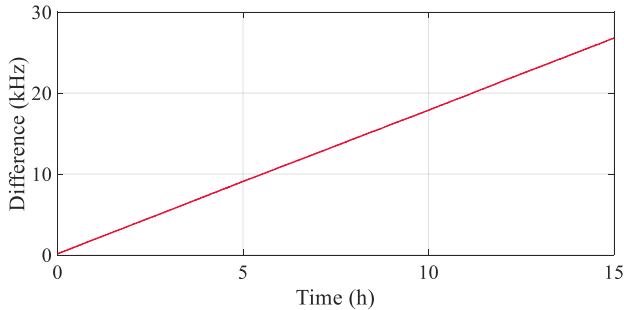


FIG. 5. Frequency difference between Alice and Bob's ultra-stable lasers. The data was recorded with two lasers placed side by side in laboratory.

2. Modulation unit

a. Wavelengths arrangement and filtering

From their electro-optical frequency combs, each user filters out three wavelength lines: λ_q (1550.495 nm), λ_c (1549.694 nm) and λ_t (1549.293 nm). The quantum wavelength λ_q has 100 GHz and 150 GHz spacings from

λ_c and λ_t , respectively. λ_q passes through the encoder and reunites with λ_c using a 50 GHz dense wavelength division multiplexing filter (DWDM). λ_t is carved by an intensity modulator (IM) and then goes through a band-pass filter with a bandwidth of 25 GHz for removal of residual λ_q light that was leaked through in the first filter. The λ_q signal is then combined with the other wavelengths through a beam splitter (BS) before transmission to Charlie through the deployed quantum channel. Their intensities are set by three variable optical attenuators (VOAs), and the λ_c and λ_t signals are set such that they produce 6 MHz and 200 kHz count rates at Charlie, respectively, such that they do not cause noticeable noise contamination to the quantum channel.

b. Encoder

Alice (Bob) applies block-wise encoding to the λ_q signal using 3 IMs and 2 phase modulators (PMs) in cascade, see Fig. 6. Within each block of 200 ns, the first 100 ns is carved into a train of 300 ps pulses at 1 ns intervals as the 'quantum signal', and each is encoded in both intensity and phase according to the requirements by the TF-QKD protocol. Four intensity levels are used, i.e., μ_Z (signal state), μ_2 (strong decoy state), μ_1 (weak decoy state) and μ_0 (vacuum state). The subsequent 100 ns in each block is carved into a single square pulse of 70 ns duration and used as the 'weak quantum reference'. A 15 ns gap at each end serves as buffer to prevent contamination to the quantum signal. IM1 is used for pulse

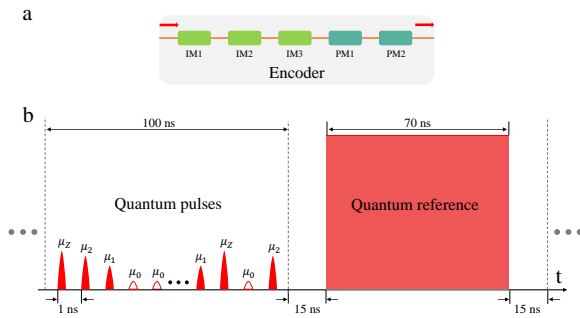


FIG. 6. Encoder (a) and the encoding sequence of the basic encoding block (b).

carving and extinguishing light transmission at vacuum time slots. IM2 produces 4-level intensity modulation and its lowest intensity setting further extinguishes the vacuum signals. IM3 is to set the intensity contrast between the ‘weak quantum reference’ and the quantum signal, with a maximum contrast of up to 700 between their integrated intensities. After intensity modulation, PM1 and PM2 encode the quantum signal pulses with 16 phase slices, $\theta \in \{0, \pi/8, 2\pi/8, \dots, 15\pi/8\}$, to meet the requirement of phase randomization and qubit encoding in TF-QKD protocol. All modulation signals are generated by an arbitrary waveform generator (Tektronix, AWG70002B). Our setup has 50 % transmission duty cycle for the quantum signals, so the effective QKD clock rate is 500 MHz. We use a 20,000-bits pseudo-random sequence for the quantum signals in the experiment, corresponding to 40 μ s duration. The encoder is capable of supporting all TF-QKD protocols.

3. Measurement units

Charlie has two measurement units (MUs), see Fig. 4 as well as in Fig. 1(b), Main Text. Coherent MU contains a 50/50 beam splitter, 2 DWDM filters and 3 superconducting nanowire single photon detectors. The incoming signals from Alice and Bob meet and interfere at the 50/50 beamsplitter, and their interference outcomes are spectrally filtered before detection. Detectors D_0 and D_1 are used to derive the raw key from quantum signal λ_q , with Detector D_0 providing also the error signal to drive the fiber stretch (FS) in the coherent dual-band stabilization. Incoherent MU consists of a polarization beam splitter, a beam splitter, DWDM and inline spectral filters, and 3 single photon detectors. It measures the incoming signals without using interference, and its measurement results are used for delay and polarization drift compensation.

4. Drifts compensation

We implement feedback controls to correct for drifts of polarization, phase, optical frequency and temporal arrivals.

a. Active polarization feedback

Charlie’s coherent MU requires the incoming optical signals to have an identical polarization so as to ensure high-visibility interference. To meet this requirement, a polarization beam splitter (PBS) is placed at each incoming fiber path before the 50/50 beam splitter. The reflected signal of λ_c and λ_q by the PBS are routed to detectors D_2 and D_3 , whose count rates are minimised to stabilize the polarization using electrically driven polarization controllers (EPC) placed at Bob (Alice). The error signal is transmitted to Alice and Bob via Internet. The communication latency (several ms) is negligible as compared to the low compensation interval (about 0.5 s). The λ_t signal also passes through the reflected path of the PBS, thanks to its polarization set perpendicular in respect to other wavelengths using a manual polarization controller (PC) in the signal path at each transmitter’ site (see Fig. 4).

b. Active phase stabilization

Coherent dual-band phase stabilization [18] we implement has two compensation stages. As shown in Fig. 4, the fast one compensates for rapid phase drift, typically at several kHz, using the count rate of D_c detector in Charlie’s coherent MU as the error signal to drive the PM in Bob’s fiber path. The slow one removes the residual phase drift using detector D_0 ’s result to adjust the FS in Alice’s fiber path. Two field-programmable-gated-arrays (FPGA1 and FPGA2) handle the two compensation stages with respective feedback rates of 100 kHz and 1 kHz.

We present a set of stabilisation results obtained over the deployed fiber link in Fig. 7. Here, we use Hz (1 Hz = 2π rad/s) to represent the phase drift rate. Panel **a** shows the fast phase drift rate with a standard deviation of 2.63 kHz. Sources for the drift include random phase fluctuation in the hundred of kilometers deployed fiber, optical frequency difference between Alice and Bob’s lasers and the finite accuracy of Rubidium clocks used in the OFC units. We extract the phase angle of λ_c and plot its distribution in Fig. 7c, which has a standard deviation of 0.25 rad. With the fast phase compensation on, the phase drift rate of λ_q is substantially slowed down. It has a standard deviation of just 12.09 Hz, as shown in Fig. 7b. We then enable FPGA2’s proportional-integral-differential (PID) controlling on the fiber stretcher (FS) to compensate the residual phase drift. Figure 7d shows

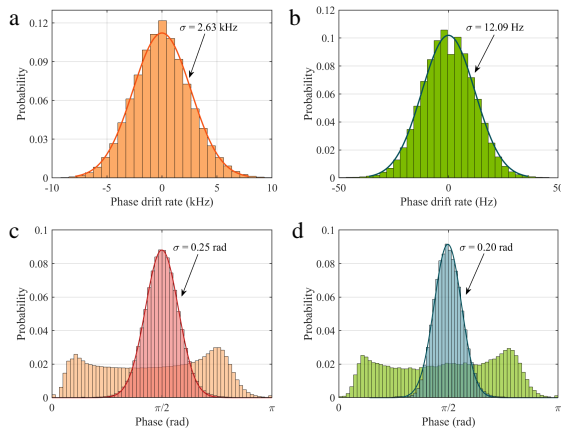


FIG. 7. Phase drift rate and the stabilization result. **a**, Histogram of the fast phase drift rate of λ_c ; **b**, Histogram of the slow residual phase drift rate of λ_q after the fast phase compensation; **c**, The phase angle distribution of the λ_c before (orange) and after (red) the channel stabilisation; **d**, The phase angle distribution of the λ_q before (green) and after (blue) the phase stabilisation. All data were measured with a time tagger in 546.61 km quantum fiber.

TABLE I. Phase stabilization results for various fiber links.

	Fiber length (km)	Free drift rate (kHz)	Fast phase stabilization (rad)	Slow phase stabilization (rad)
Symmetric	546.61	2.63	0.25	0.20
	603.87	2.11	0.23	0.23
Asymmetric	452.46	2.14	0.24	0.25

the histogram of angle distribution of the λ_q signal to have a standard deviation of 0.20 rad.

The phase drift rates and the corresponding stabilization results for different fiber links are summarized in Table I.

c. Frequency compensation

To allow real-time frequency compensation, an acoustic-optic modulator (AOM) is placed between Alice's ultrastable laser and the electro-optic modulator in her OFC unit. Based on the measurement of the linear frequency drift between the lasers in the users' OFC units (see Fig. 5), we preset accordingly a compensating shift in the AOM's driving frequency. We measure the effect of this frequency pre-compensation in laboratory and the result is shown in Fig. 8. Within 20 h, the two lasers' frequency difference stays within ± 300 Hz, a difference that is one order of magnitude smaller than fluctuation caused by the deployed fiber and can thus be corrected for by the coherent dual-band stabilization.

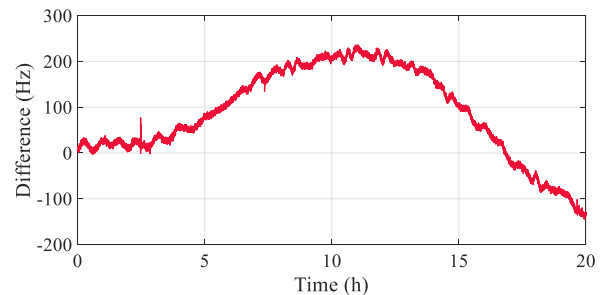


FIG. 8. Differential frequency between two independent lasers with compensation.

d. Time compensation

To synchronize Alice and Bob's modulation units, Charlie distributes a 50 MHz clock signal to Alice and Bob through the clock synchronization channel, see Fig. 9. A total of four erbium doped fiber amplifiers (EDFAs) are used to ensure sufficient optical power reaching the destinations. The detailed locations of these EDFAs are as the following, Bogeyan town ($117^{\circ}62'$ E, $36^{\circ}39'$ N), Yiyuan City ($118^{\circ}12'$ E, $36^{\circ}11'$ N), Zhucheng city ($119^{\circ}24'$ E, $36^{\circ}2'$ N) and Huangshan city ($119^{\circ}99'$ E, $36^{\circ}17'$ N). At each user's site, the 50 MHz optical signal is converted to an electrical clock by a photodiode. The delays (Δt_A and Δt_B) of these clocks are adjusted in real time by Charlie based on his measurement of the arrivals of λ_t pulses sent by Alice and Bob using the D_t detector in his incoherent MU. This is to ensure optimal alignment between Alice and Bob's quantum pulses and thus high visibility interference.

5. Quantum channel and system loss characterization

The deployed fiber link is formed by ultra-low-loss fiber (G654.E ULL). The buried fiber from Alice (Bob) to Charlie is 223.01 km (204.22 km) with a loss of 42.40 dB (37.77 dB), while the physical separation between Alice and Bob is about 300 km. In Charlie's side, fiber spools (G654.C ultra-low-loss fiber) with a typical loss coefficient of 0.160 dB km^{-1} are included to vary the length of quantum channel, which is characterised to have an average loss coefficient ranging from 0.180 dB km^{-1} to 0.187 dB km^{-1} in the experiments. We summarize the lengths and corresponding losses for the quantum channel in Table II.

Table III summarizes losses of a series of components with respect to each user's input port in Charlie's module. Charlie's transmission loss for Bob's quantum signal is 4.73 dB, which is 0.92 dB higher than Alice's because of the loss by the phase modulator. This loss asymmetry is compensated for with fibers in the experiments of symmetric configuration. The characteristics of superconducting nanowire single photon detectors (SNSPDs)

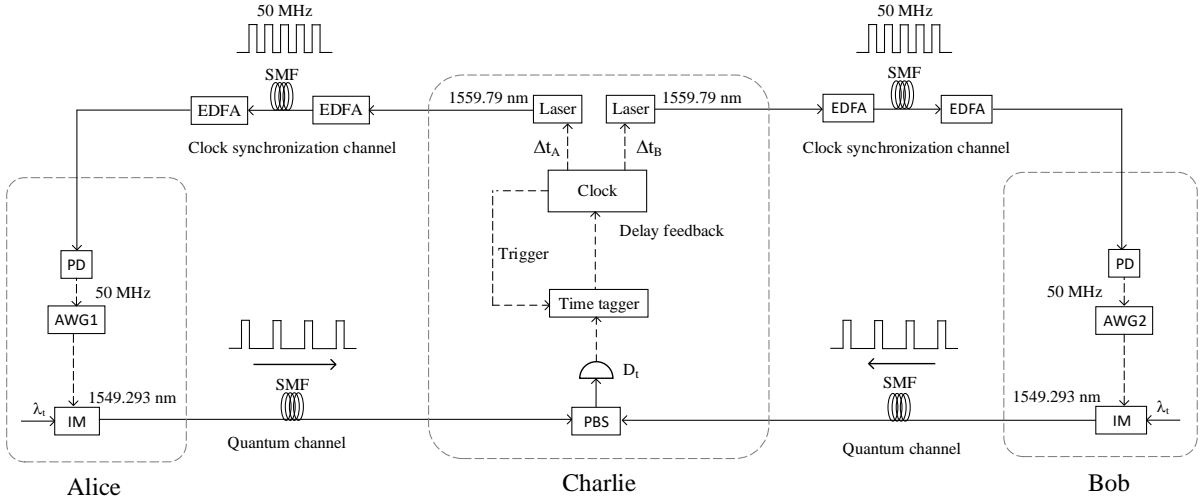


FIG. 9. Clock synchronization and delay feedback setup. In Charlie the clock is used to synchronize his own time tagger locally. Charlie distributes two 50 MHz optical pulses through clock synchronization channel to synchronize the AWGs in Alice and Bob. AWG: arbitrary waveform generator; SMF: single mode fiber; PBS: polarization beam combiner; PD: photodiode; EDFA: Erbium-doped optical fiber amplifier; SNSPD: superconducting nanowire single photon detector; IM: intensity modulator.

TABLE II. Lengths and corresponding losses for the fiber links we used in the experiments.

	Total		Alice		Bob	
	length (km)	loss (dB)	length (km)	loss (dB)	length (km)	loss (dB)
Symmetric	546.61	100.13	273.48	50.50	273.13	49.63
	603.87	108.59	298.71	54.74	305.16	53.85
Asymmetric	452.46	84.62	248.24	46.85	204.22	37.77

are presented in Table IV. The detector dark count rate was measured in field under the condition that the λ_c (λ_t) light produces 6 MHz (200 kHz) count rate at detector D_c (D_t). The scattered noise from λ_c is capped below 1 Hz thanks to the excellent channel isolation [18]. For the 603 km fiber experiment, we decrease the bias current in the detectors to further suppress the dark counts at expense of detection efficiencies.

TABLE III. Charlie's components loss.

	Alice	Bob
Polarisation beam splitter	0.47	0.49
Phase modulator	n/a	1.97
Fiber stretch and filter	1.05	n/a
50/50 beam splitter	0.66	0.65
DWDM filter	1.20	1.20
Polarisation controller	0.15	0.15
Optical switch	0.28	0.27
Total loss (dB)	3.81	4.73

Appendix C: Detailed experimental parameters and results

Table V lists the encoding parameters used in the symmetric and asymmetrical experiments. Alice and Bob share the same parameters in the symmetric experiment. P_Z (P_X) is the probability of encoding a pulse in the Z (X) basis. In the time window of Z basis, weak coherent pulses with signal (μ_Z) and vacuum (μ_0) intensities are randomly prepared with probability ϵ and $1 - \epsilon$. While in the X basis, weak coherent pulses with strong decoy (μ_2), weak decoy (μ_1) and vacuum (μ_0) intensities are randomly prepared with the corresponding probabilities p_{μ_2} , p_{μ_1} and p_{μ_0} , respectively. $P_Z + P_X = 1$ and $p_{\mu_2} + p_{\mu_1} + p_{\mu_0} = 1$.

Table VI summarizes the experimental results and parameters that are useful for secure key rate (SKR) calculation. N is the total number of transmitted quantum pulses. The numbers of successful clicks recorded in Charlie are list as “Detected AB_{ab} ”, where “A” (“B”) indicates the X (Z) basis that Alice or Bob uses, and “a” (“b”) is 0, 1, 2 or 3 representing the chosen intensity μ_0 , μ_1 , μ_2 or μ_Z . QBER (X_{11}) and QBER (X_{22}) indicate the error rate when Alice and Bob both send decoy state μ_1 and μ_2 in the X basis, respectively. SKC_0 is the ab-

TABLE IV. Characteristics of Charlie's detectors D_0 and D_1 in different fiber lengths.

Detector	Efficiency	Dark Count	Efficiency (603 km)	Dark Count (603 km)
D_0	83 %	7.80 Hz	70 %	4.15 Hz
D_1	49 %	1.77 Hz	47 %	1.18 Hz

solute repeaterless Pirandola-Laurenza-Ottaviani-Banchi (PLOB) bound. The rest of the notations see the Section I.

TABLE V. Encoding parameters used in the symmetric and asymmetrical setups.

Parameter	Symmetric		Asymmetric	
	546.61km	603.87km	452.46km	
	Alice/Bob	Alice/Bob	Alice	Bob
μ_Z	0.493	0.423	0.493	0.247
μ_2	0.493	0.252	0.493	0.077
μ_1	0.090	0.056	0.113	0.018
μ_0	0.0002	0.0002	0.0002	0.0002
P_Z	0.735		0.735	0.735
P_X	0.265		0.265	0.265
ϵ	0.269		0.405	0.141
p_{μ_2}	0.316		0.316	0.316
p_{μ_1}	0.606		0.606	0.606
p_{μ_0}	0.078		0.078	0.078

-
- [1] C. H. Bennett and G. Brassard, Quantum cryptography: Public key distribution and coin tossing, *Theor. Comput. Sci.* **560**, 7 (2014).
- [2] M. Peev, C. Pacher, R. Alléaume, C. Barreiro, J. Bouda, W. Boxleitner, T. Debuisschert, E. Diamanti, M. Dianati, J. F. Dynes, S. Fasel, S. Fossier, M. Fürst, J.-D. Gautier, O. Gay, N. Gisin, P. Grangier, A. Happe, Y. Hasani, M. Hentschel, H. Hübel, G. Humer, T. Länger, M. Legré, R. Lieger, J. Lodewyck, T. Lorünser, N. Lütkenhaus, A. Marhold, T. Matyus, O. Maurhart, L. Monat, S. Nauerth, J.-B. Page, A. Poppe, E. Querasser, G. Ribordy, S. Robyr, L. Salvail, A. W. Sharpe, A. J. Shields, D. Stucki, M. Suda, C. Tamas, T. Themel, R. T. Thew, Y. Thoma, A. Treiber, P. Trinkler, R. Tualle-Brouiri, F. Vannel, N. Walenta, H. Weier, H. Weinfurter, I. Wimberger, Z. L. Yuan, H. Zbinden, and A. Zeilinger, The SECOQC quantum key distribution network in Vienna, *New J. Phys.* **11**, 075001 (2009).
- [3] M. Sasaki, M. Fujiwara, H. Ishizuka, W. Klaus, K. Wakui, M. Takeoka, S. Miki, T. Yamashita, Z. Wang, A. Tanaka, K. Yoshino, Y. Nambu, S. Takahashi, A. Tajima, A. Tomita, T. Domeki, T. Hasegawa, Y. Sakai, H. Kobayashi, T. Asai, K. Shimizu, T. Tokura, T. Tsurumaru, M. Matsui, T. Honjo, K. Tamaki, H. Takesue, Y. Tokura, J. F. Dynes, A. R. Dixon, A. W. Sharpe, Z. L. Yuan, A. J. Shields, S. Uchikoga, M. Legré, S. Robyr, P. Trinkler, L. Monat, J.-B. Page, G. Ribordy, A. Poppe, A. Allacher, O. Maurhart, T. Länger, M. Peev, and A. Zeilinger, Field test of quantum key distribution in the Tokyo QKD Network, *Opt. Express* **19**, 10387 (2011).
- [4] J. F. Dynes, A. Wonfor, W. W.-S. Tam, A. W. Sharpe, R. Takahashi, M. Lucamarini, A. Plews, Z. L. Yuan, A. R. Dixon, J. Cho, A. R. Dixon, Y. Tanizawa, R. Pentyl, and A. J. Shields, Cambridge quantum network, *npj Quant. Inf.* **5**, 101 (2019).
- [5] Y.-A. Chen, Q. Zhang, T.-Y. Chen, W.-Q. Cai, S.-K. Liao, J. K. Chen, J. Yin, J.-G. Ren, Z. Chen, S.-L. Han, Q. Yu, K. Liang, F. Zhou, X. Yuan, M.-S. Zhao, T.-Y. Wang, X. Jiang, L. Zhang, W.-Y. Liu, Y. Li, Q. Shen, Y. Cao, C.-Y. Lu, R. Shu, J.-Y. Wang, L. Li, N.-L. Liu, F. Xu, X.-B. Wang, C.-Z. Peng, and J.-W. Pan, An integrated space-to-ground quantum communication network over 4,600 kilometres, *Nature* **589**, 214 (2021).
- [6] D. Ribezzo, M. Zahidy, I. Vagniluca, N. Biagi, S. Francesconi, T. Occhipinti, L. K. Oxenløwe, M. Lončarić, I. Cvitić, M. Stipčević, . Pušavec, R. Kaltenbaek, A. Ramšak, F. Cesa, G. Giorgetti, F. Scazza, A. Bassi, P. De Natale, F. S. Cataliotti, M. Inguscio, D. Bacco, and A. Zavatta, Deploying an inter-European quantum network, *Adv. Quant. Technol.* **6**, 2200061 (2023).
- [7] E. Bersin, M. Grein, M. Sutula, R. Murphy, Y. Q. Huan, M. Stevens, A. Suleymanzade, C. Lee, R. Riedinger, D. J. Starling, P.-J. Stas, C. M. Knaut, N. Sinclair, D. R. Assumpcao, Y.-C. Wei, E. N. Knall, B. Machielse, D. D. Sukachev, D. S. Levonian, M. K. Bhaskar, M. Lončar, S. Hamilton, M. Lukin, D. Englund, and P. B. Dixon,

TABLE VI. Experimental results at various quantum link fiber lengths with SNS-AOPP-TF-QKD protocol.

Total length (km)	546.61	603.87	452.46
Alice-Charlie (km)	273.48	298.71	248.24
Bob-Charlie (km)	273.13	305.16	204.22
N	2.772×10^{13}	4.05×10^{12}	4.28×10^{12}
Detected XX_{20}	68859	1856	23105
Detected XX_{02}	67693	2162	21269
Detected XX_{10}	29156	878	9097
Detected XX_{01}	24569	1163	8878
Detected XX_{00}	63	7	21
Detected XZ_{00}	1847	195	363
Detected XZ_{10}	649804	24830	198482
Detected XZ_{20}	1805364	60929	443226
Detected ZX_{00}	1924	220	496
Detected ZX_{01}	621437	26334	320369
Detected ZX_{02}	1787060	57269	707987
Detected ZZ_{03}	4005761	234768	2556562
Detected ZZ_{30}	4396652	245490	1708076
Detected ZZ_{33}	3107361	177447	1549556
Detected ZZ_{00}	51305	5757	10474
QBER (X_{11})	8.71%	8.50%	6.87%
QBER (X_{22})	9.63%	8.82%	6.75%
QBER (E_z before AOPP)	27.32%	27.61%	26.38%
QBER (E_z after AOPP)	0.90%	1.74%	0.37%
n_1 (Before AOPP)	4.901×10^6	2.932×10^5	2.774×10^6
n_1 (After AOPP)	7.995×10^5	5.061×10^4	5.893×10^5
e_1^{ph} (Before AOPP)	11.28%	7.90%	9.94%
e_1^{ph} (After AOPP)	20.01%	14.55%	17.90%
SKR (bit/s) - finite size	0.53	/	16.06
SKR (bit/signal) - finite size	1.060×10^{-9}	/	3.212×10^{-8}
SKR (bit/s) - asymptotic	/	0.12	/
SKR (bit/signal) - asymptotic	/	2.455×10^{-10}	/
SKC ₀ (bit/signal)	1.400×10^{-10}	1.996×10^{-11}	4.979×10^{-9}
Ratio SKR over SKC ₀	7.57	12.30	6.45

Development of a Boston-area 50-km fiber quantum network testbed, Phys. Rev. Appl. **21**, 014024 (2024).

- [8] Z. Yuan, A. Plews, R. Takahashi, K. Doi, W. Tam, A. W. Sharpe, A. R. Dixon, E. Lavelle, J. F. Dynes, A. Murakami, M. Kujiraoka, M. Lucamarini, Y. Tanizawa, H. Sato, and A. J. Shields, 10-Mb/s quantum key distribution, J. Lightwave Technol. **36**, 3427 (2018).
- [9] W. Li, L. Zhang, H. Tan, Y. Lu, S.-K. Liao, J. Huang, H. Li, Z. Wang, H.-K. Mao, B. Yan, Q. Li, Y. Liu, Q. Zhang, C.-Z. Peng, L. You, F. Xu, and J.-W. Pan, High-rate quantum key distribution exceeding 110 Mb s⁻¹, Nat. Photon. **17**, 416 (2023).
- [10] F. Grünenfelder, A. Boaron, G. V. Resta, M. Perrenoud, D. Rusca, C. Barreiro, R. Houlmann, R. Sax, L. Stasi, S. El-Khoury, E. Hänggi, N. Bosshard, F. Bussi eres, and H. Zbinden, Fast single-photon detectors and real-time key distillation enable high secret-key-rate quantum key distribution systems, Nat. Photon. **17**, 422 (2023).
- [11] A. Boaron, G. Boso, D. Rusca, C. Vulliez, C. Autebert, M. Caloz, M. Perrenoud, G. Gras, F. Bussi eres, M.-J. Li, D. Nolan, A. Martin, and H. Zbinden, Secure quantum key distribution over 421 km of optical fiber, Phys. Rev. Lett. **121**, 190502 (2018).
- [12] M. Lucamarini, Z. L. Yuan, J. F. Dynes, and A. J. Shields, Overcoming the rate–distance limit of quantum key distribution without quantum repeaters, Nature **557**, 400 (2018).
- [13] P. Zeng, H. Zhou, W. Wu, and X. Ma, Mode-pairing quantum key distribution, Nat. Commun. **13**, 3903 (2022).
- [14] Y.-M. Xie, Y.-S. Lu, C.-X. Weng, X.-Y. Cao, Z.-Y. Jia, Y. Bao, Y. Wang, Y. Fu, H.-L. Yin, and Z.-B. Chen, Breaking the rate-loss bound of quantum key distribution with asynchronous two-photon interference, PRX Quantum **3**, 020315 (2022).
- [15] J.-P. Chen, C. Zhang, Y. Liu, C. Jiang, W. Zhang, X.-L. Hu, J.-Y. Guan, Z.-W. Yu, H. Xu, J. Lin, M.-J. Li, H. Chen, H. Li, L. You, Z. Wang, X.-B. Wang, Q. Zhang, and J.-W. Pan, Sending-or-not-sending with independent lasers: secure twin-field quantum key distribution over 509 km, Phys. Rev. Lett. **124**, 070501 (2020).
- [16] M. Pittaluga, M. Minder, M. Lucamarini, M. Sanzaro, R. I. Woodward, M.-J. Li, Z. Yuan, and A. J. Shields, 600-km repeater-like quantum communications with dual-band stabilization, Nat. Photon. **15**, 530 (2021).
- [17] S. Wang, Z.-Q. Yin, D.-Y. He, W. Chen, R.-Q. Wang, P. Ye, Y. Zhou, G.-J. Fan-Yuan, F.-X. Wang, W. Chen, Y.-G. Zhu, P. V. Morozov, A. V. Divochiy, Z. Zhou, G.-C. Guo, and Z.-F. Han, Twin-field quantum key distribution

- over 830-km fibre, *Nat. Photon.* **16**, 154 (2022).
- [18] L. Zhou, J. Lin, Y. Jing, and Z. Yuan, Twin-field quantum key distribution without optical frequency dissemination, *Nat. Commun.* **14**, 928 (2023).
- [19] Y. Liu, W.-J. Zhang, C. Jiang, J.-P. Chen, C. Zhang, W.-X. Pan, D. Ma, H. Dong, J.-M. Xiong, C.-J. Zhang, *et al.*, Experimental twin-field quantum key distribution over 1000 km fiber distance, *Phys. Rev. Lett.* **130**, 210801 (2023).
- [20] L. Zhou, J. Lin, Y.-M. Xie, Y.-S. Lu, Y. Jing, H.-L. Yin, and Z. Yuan, Experimental quantum communication overcomes the rate-loss limit without global phase tracking, *Phys. Rev. Lett.* **130**, 250801 (2023).
- [21] H.-K. Lo, M. Curty, and B. Qi, Measurement-device-independent quantum key distribution, *Phys. Rev. Lett.* **108**, 130503 (2012).
- [22] H. Liu, C. Jiang, H.-T. Zhu, M. Zou, Z.-W. Yu, X.-L. Hu, H. Xu, S. Ma, Z. Han, J.-P. Chen, Y. Dai, S.-B. Tang, W. Zhang, H. Li, L. You, Z. Wang, Y. Hua, H. Hu, H. Zhang, F. Zhou, Q. Zhang, X.-B. Wang, T.-Y. Chen, and J.-W. Pan, Field test of twin-field quantum key distribution through sending-or-not-sending over 428 km, *Phys. Rev. Lett.* **126**, 250502 (2021).
- [23] J.-P. Chen, C. Zhang, C. Liu, Yang Jiang, W.-J. Zhang, Z.-Y. Han, S.-Z. Ma, X.-L. Hu, Y.-H. Li, F. Liu, Hui Zhou, H.-F. Jiang, H. Chen, Teng-Yun Li, L.-X. You, Z. Wang, X.-B. Wang, Q. Zhang, and J.-W. Pan, Twin-field quantum key distribution over a 511 km optical fibre linking two distant metropolitan areas, *Nat. Photon.* **15**, 570 (2021).
- [24] C. Clivati, A. Meda, S. Donadello, S. Virzi, M. Genovese, F. Levi, A. Mura, M. Pittaluga, Z. Yuan, A. J. Shields, M. Lucamarini, I. P. Degiovanni, and D. Calonico, Coherent phase transfer for real-world twin-field quantum key distribution, *Nat. Commun.* **13**, 157 (2022).
- [25] X.-B. Wang, Z.-W. Yu, and X.-L. Hu, Twin-field quantum key distribution with large misalignment error, *Phys. Rev. A* **98**, 062323 (2018).
- [26] X.-L. Hu, C. Jiang, Z.-W. Yu, and X.-B. Wang, Sending-or-not-sending twin-field protocol for quantum key distribution with asymmetric source parameters, *Phys. Rev. A* **100**, 062337 (2019).
- [27] H. Xu, Z.-W. Yu, C. Jiang, X.-L. Hu, and X.-B. Wang, Sending-or-not-sending twin-field quantum key distribution: Breaking the direct transmission key rate, *Phys. Rev. A* **101**, 042330 (2020).
- [28] C. Jiang, X.-L. Hu, H. Xu, Z.-W. Yu, and X.-B. Wang, Zigzag approach to higher key rate of sending-or-not-sending twin field quantum key distribution with finite-key effects, *New J. Phys.* **22**, 053048 (2020).
- [29] S. Pirandola, R. Laurenza, C. Ottaviani, and L. Banchi, Fundamental limits of repeaterless quantum communications, *Nat. Commun.* **8**, 15043 (2017).
- [30] B. Amies-King, K. P. Schatz, H. Duan, A. Biswas, J. Bailey, A. Felvinti, J. Winward, M. Dixon, M. Minder, R. Kumar, S. Albosh, and M. Lucamarini, Quantum communications feasibility tests over a UK-Ireland 224 km undersea link, *Entropy* **25**, 1572 (2023).
- [31] S. P. Neumann, A. Buchner, L. Bulla, M. Bohmann, and R. Ursin, Continuous entanglement distribution over a transnational 248 km fiber link, *Nat. Commun.* **13**, 6134 (2022).
- [32] C. M. Knaut, A. Suleymanzade, Y.-C. Wei, D. R. Assumpcao, P.-J. Stas, Y. Q. Huan, B. Machielse, E. N. Knall, M. Sutula, G. Baranes, N. Sinclair, C. De-Eknamkul, D. S. Levonian, M. K. Bhaskar, H. Park, M. Lončar, and M. D. Lukin, Entanglement of nanophotonic quantum memory nodes in a telecommunication network, *Nature* **629**, 573 (2024).
- [33] J.-L. Liu, X.-Y. Luo, Y. Yu, C.-Y. Wang, B. Wang, Y. Hu, J. Li, M.-Y. Zheng, B. Yao, Z. Yan, D. Teng, J.-W. Jiang, X.-B. Liu, X.-P. Xie, J. Zhang, Q.-H. Mao, X. Jiang, Q. Zhang, X.-H. Bao, and J.-W. Pan, A multi-node quantum network over a metropolitan area, *Nature* **629**, 579 (2024).
- [34] Optically pumped miniaturised Cs atomic clock, high performance version, see <https://shop.stepglobal.com/documents/productpdf/TA1000-M1.pdf>.
- [35] Z. Yan, T. Shi, Y. Fan, L. Zhou, and Z. Yuan, Compact InGaAs/InP single-photon detector module with ultranarrowband interference circuits, *Adv. Dev. Instrum.* **4**, 0029 (2023).
- [36] Z.-W. Yu, X.-L. Hu, C. Jiang, H. Xu, and X.-B. Wang, Sending-or-not-sending twin-field quantum key distribution in practice, *Sci. Rep.* **9**, 3080 (2019).
- [37] C. Jiang, X.-L. Hu, Z.-W. Yu, and X.-B. Wang, Composable security for practical quantum key distribution with two way classical communication, *New J. Phys.* **23**, 063038 (2021).
- [38] A. Vitanov, F. Dupuis, M. Tomamichel, and R. Renner, Chain rules for smooth min- and max-entropies, *IEEE Trans. Inf. Theor.* **59**, 2603 (2013).